AGU PUBLICATIONS

JGR

Journal of Geophysical Research: Space Physics

RESEARCH ARTICLE
10.1002/2014JA019991

Key Points:
- Electron holes are found in the separatrix region
- The EHs are located at the border between the electron inflow and outflow
- The detail about the formation and evolution of these EHs is represented

Supporting Information:
- Readme
- Animation S1

Correspondence to:
Q. Lu,
qmlu@ustc.edu.cn

Citation:
Huang, C., Q. Lu, P. Wang, M. Wu, and S. Wang (2014), Characteristics of electron holes generated in the separatrix region during antiparallel magnetic reconnection, *J. Geophys. Res. Space Physics*, *119*, 6445–6454, doi:10.1002/2014JA019991.

Received 20 MAR 2014
Accepted 5 AUG 2014
Accepted article online 11 AUG 2014
Published online 22 AUG 2014

Characteristics of electron holes generated in the separatrix region during antiparallel magnetic reconnection

Can Huang[1], Quanming Lu[1], Peiran Wang[1], Mingyu Wu[1], and Shui Wang[1]

[1]CAS Key Laboratory of Geospace Environment, Department of Geophysics and Planetary Science, University of Science and Technology of China, Hefei, China

Abstract In this paper, two-dimensional particle-in-cell simulations are performed to investigate the characteristics of these electron holes generated in the separatrix region of antiparallel magnetic reconnection. The electron holes with bipolar structures of the parallel electric field are formed in the border between the electron inflow channel (where electrons move toward the X line) and outflow channel (where electrons flow away from the X line), where the electrons satisfy the bump-on-tail distribution. Quasi-monochromatic electrostatic waves, which propagate with a speed near the bulk velocity of the fast electron beam, are first excited by the electron bump-on-tail instability. These waves then coalesce with each other, and at last electron holes are formed in the separatrix region which then propagate away from the X line along the magnetic field lines.

1. Introduction

Electrostatic solitary structures are commonly observed in different space environments, such as the plasma sheet [*Matsumoto et al*., 1994], the auroral region [*Ergun et al*., 1998], magnetosheath [*Pickett et al*., 2004], magnetopause [*Cattell et al*., 2002], and the solar wind [*Mangeney et al*., 1999]. In general, such electrostatic structures show positive potential pulses, and their parallel electric field (the component of the electric field, which is parallel to the background magnetic field) has bipolar signatures. They are proposed to be closely related to electron phase-space holes (electron holes). From a theoretical view, electron holes are considered to be the stationary Bernstein-Greene-Kruskal solution of Vlasov and Poisson equations [*Bernstein et al*., 1957; *Muschietti et al*., 1999; *Chen et al*., 2005; *Ng and Bhattacharjee*, 2005]. Particle-in-cell (PIC) simulations have found that electron holes can be formed during the nonlinear evolution of the electron streaming instabilities (caused by the relative drift between different electron populations) or Buneman instability (caused by the relative drift between ions and electrons) [*Morse and Nielson*, 1969; *Omura et al*., 1994; *Mottez et al*., 1997; *Lu et al*., 2005a, 2005b]. Recently, electron holes associated with magnetic reconnection have been observed in the magnetotail and laboratory [*Cattell et al*., 2005; *Fox et al*., 2008; *Khotyaintsev et al*., 2010]. The bipolar structure of the parallel electric field associated with the electron holes is considered to be a diagnostic for reconnection events in satellite observations [*Lapenta et al*., 2011]. Whistlers can be strongly excited by electron holes. When they pass near the X line, the reconnection rate can be modulated [*Goldman et al*., 2014].

Although it is generally accepted that streaming instabilities lead to the generation of electron holes in magnetic reconnection, the exact mechanism is still under debate. In three-dimensional PIC simulations of magnetic reconnection with a strong guide field, *Drake et al*. [2003] found that electron holes can be formed near the X line due to the Buneman instability by the relative drift between ions and electrons, and these electron holes propagate along the out-of-plane direction (parallel to the guide field). These electron holes can lead to strong electron scattering, which is necessary for the expedition of fast reconnection. In the works of *Che et al*. [2009], besides the electron holes that formed during the nonlinear development of the Buneman instability, the turbulence associated with the parallel electron-electron two-stream instability and the nearly perpendicular lower hybrid instability is also driven. By performing one-dimensional (1-D) and two-dimensional (2-D) electrostatic Vlasov simulations with parallel velocity particle distributions taken from 2-D PIC simulations of magnetic reconnection with a guide field, *Goldman et al*. [2008] demonstrated that the electron holes in the separatrix region (the region around the separatrices, and the width is about one ion

inertial length) are resulted from the Buneman instability, while near the X line both the Buneman instability and electron streaming instability may lead to electron holes. In 2-D PIC simulations of magnetic reconnection with a guide field, *Lapenta et al*. [2010, 2011] attributed the generated electron holes in the separatrix region to the Buneman instability, and the relative drift between ions and electrons is formed due to the observed fast electron flow toward the X line within the electron density cavities. However, *Pritchett and Coroniti* [2004] indicated that an electron streaming instability may also be unstable in the separatrix region during a guide field reconnection, and then its nonlinear evolution generates electron holes. With 2-D PIC simulations, *Fujimoto and Machida* [2006] also found the existence of electron holes in the plasma sheet-lobe boundary region during antiparallel magnetic reconnection. These electron holes are formed due to the cold electron two-stream instability between the background cold electrons and the intense beam electrons flowing away from the X line. In antiparallel magnetic reconnection, electrons stream toward the X line along the separatrices and then leave the X line along the magnetic field lines just inside the separatrices after they are accelerated by the reconnection electric field in the vicinity of the X line [*Hoshino et al*., 2001; *Huang et al*., 2010; *Lu et al*., 2010]. In this paper, by performing 2-D PIC simulations of antiparallel magnetic reconnection, we investigate the detailed characteristics of the electron holes generated in the separatrix region during antiparallel magnetic reconnection. The electron holes exist in the border between the electron inflow channel (where electrons move toward the X line) and outflow channel (where electrons flow away from the X line), where the electrons satisfy the bump-on-tail distribution. Quasi-monochromatic electrostatic waves are first excited due to the electron bump-on-tail instability, and they coalesce with each other in the nonlinear evolution stage until several electron holes with the bipolar structures of the parallel electric field are at last formed. These electron holes propagate away from the X line along the magnetic field lines with a speed near the bulk velocity of the fast electron outflow.

The structure of the paper is as follows. In section 2, the simulation model is overviewed. The simulation results are presented in section 3. The conclusions and discussion are given in section 4.

2. Simulation Model

Two-dimensional PIC simulations are carried out in this paper to investigate the generation of electron holes during antiparallel magnetic reconnection. In the simulation model, the electromagnetic fields are defined on the grids and updated by integrating the Maxwell equations with an explicit leapfrog algorithm, and the ions and electrons are treated as individual particles and advanced in the electromagnetic field. Periodic boundary conditions are assumed in the x direction, while in the z direction conducting boundary conditions are retained and particles are specularly reflected. The initial equilibrium configuration is described as a 1-D Harris current sheet with the expression $\mathbf{B}(z) = B_0 \tanh(z/\delta)\mathbf{e}_x$, where δ is the half width of the current sheet and B_0 is the asymptotical magnetic field. δ is chosen as $\delta = 0.5c/\omega_{pi}$ (where c/ω_{pi} is the ion inertial length based on the peak Harris number density n_0). The corresponding number density have the form $n(z) = n_b + n_0 \mathrm{sech}^2(z/\delta)$, where $n_b = 0.2n_0$ represents the background density. Ions and electrons are assumed to satisfy the Maxwellian distribution, and the initial temperature ratio is set as $T_{i0}/T_{e0} = 4$. The mass ratio is set to be $m_i/m_e = 64$ (where m_i/m_e is the rest mass of the ion/electron), and the light speed is $c = 30V_A$, where V_A is the Alfven speed based on B_0 and n_0. The initial thermal velocities of the ions and electrons are about 0.8 V_A and 2 V_A, while the gyroradius of the ion and electron are about 0.8 c/ω_{pi} and 0.02 c/ω_{pi}. The gyrofrequency/plasma frequency ratio is $\Omega_i/\omega_{pi} = V_A/c = 1/30$. The (x, z) plane is the simulation domain. The computational domain size is $L_x \times L_z = 51.2c/\omega_{pi} \times 12.8c/\omega_{pi}$ with the spatial resolution $\Delta x = \Delta z = 0.05c/\omega_{pi}$. The time step is set to be $\Delta t = 0.001\Omega_i^{-1}$, where $\Omega_i = eB_0/m_i$ is the ion gyrofrequency. More than 300 million particles are employed in the simulation domain. Reconnection is initiated by a small flux perturbation.

3. Simulation Results

The evolution of the magnetic reconnection is snapshotted in Figure 1. The left and right show the parallel electric field $E_{||}/V_A B_0$ and parallel electron bulk velocity $V_{e||}/V_A$ at $\Omega_i t = 26.2$, 28.8, and 31.4, respectively. Here the in-plane magnetic field lines are also presented for reference. With the growth of the reconnection, an X line occurs around $x = 27c/\omega_{pi}$. As reported in the previous works, the electrons move toward the X line along the separatrices and get accelerated in the vicinity of the X line and then flow out along the magnetic field lines [*Hoshino et al*., 2001; *Huang et al*., 2010; *Lu et al*., 2010]. Around $\Omega_i t = 28.8$, the bipolar structures of the parallel electric field begin to appear in the separatrix region. As the time goes on, the electron

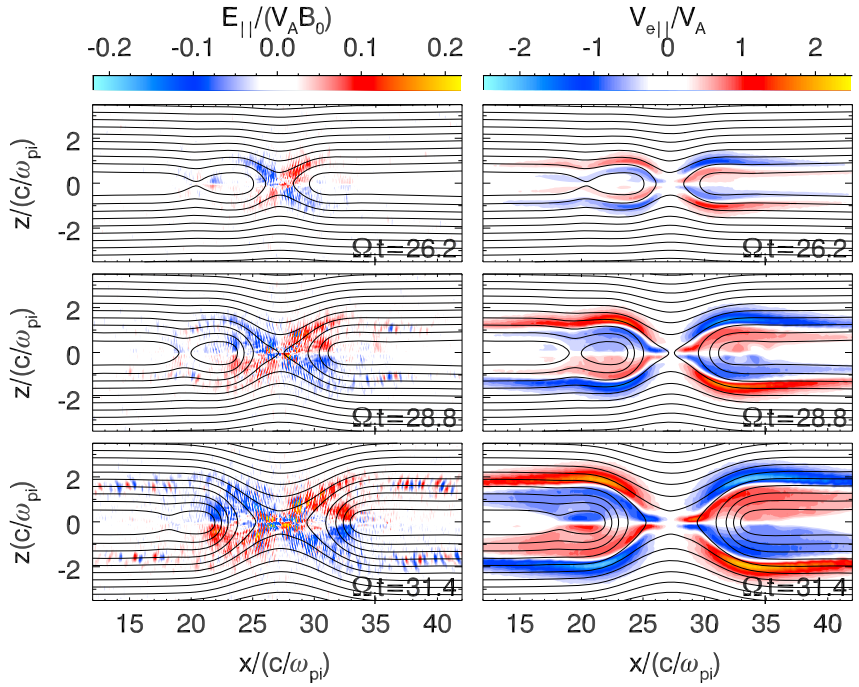

Figure 1. The time evolution of the (left) parallel electric field $E_{||}/V_AB_0$ and (right) electron parallel bulk velocity $V_{e||}/V_A$ at $\Omega_i t$ = 26.2, 28.8, and 31.4 from top to bottom. The in-plane magnetic field lines are presented.

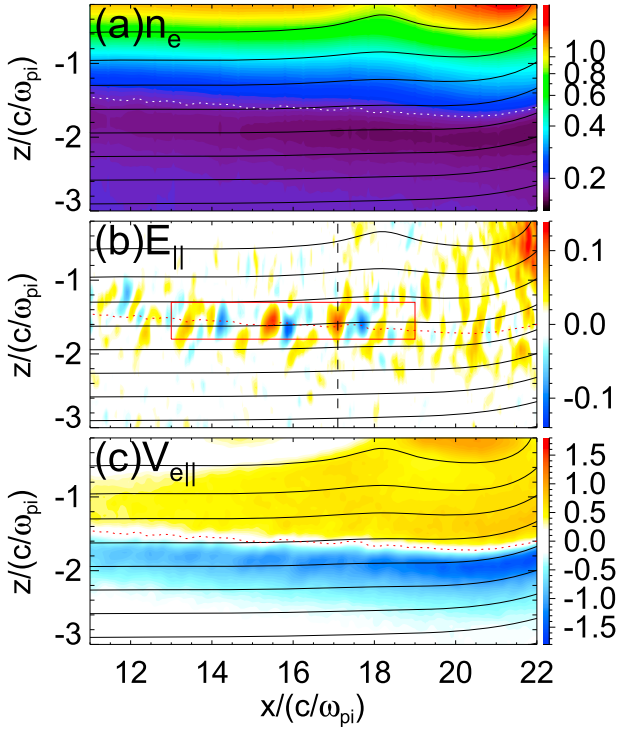

Figure 2. The (a) electron number density n_e/n_0, (b) parallel electric field $E_{||}/V_AB_0$, and (c) electron parallel bulk velocity $V_{e||}/V_A$ at $\Omega_i t$ = 31.4. The in-plane magnetic field lines are presented. The dotted curves mark the border between the electron inflow and outflow channels.

bulkflow become stronger, and the region with the parallel electric field $E_{||}$ extends along the magnetic field lines around the separatrices. At $\Omega_i t$ = 31.4, the bipolar structures of the parallel electric field are well developed in the separatrix region. The supporting information includes a video of the evolution of $E_{||}$, which illustrates very clearly the generation and propagation of the bipolar structures in the separatrix region during reconnection. Please note that a long initial current sheet is used in our simulations, and only a single X line occurs. This allows us to trace the structures of the electric field before the computational boundary can have an effect on the electric field and electron bulk flow near the separatrices. After comparing the structures of the electric field and electron bulk velocity, we can find that the bipolar structures of electric field are roughly located in the border between the electron inflow and outflow channels. This can be distinguished more clearly in Figures 2 and 3. Figure 2 plots the distributions of (a) the electron number density n_e/n_0, (b) the parallel

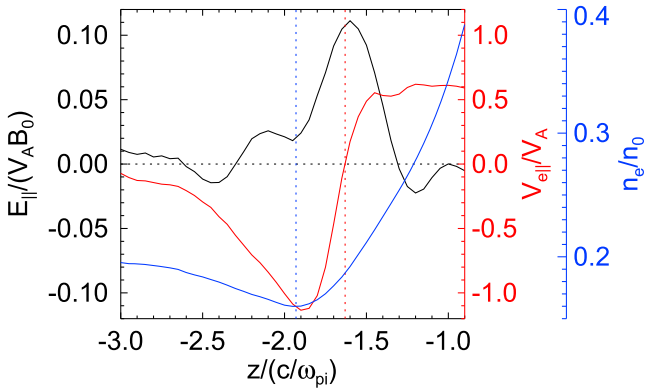

Figure 3. The profiles of the parallel electric field $E_{||}/V_AB_0$ (black), electron parallel bulk velocity $V_{e||}/V_A$ (red), and electron number density n_e/n_0 (blue). The red dashed line denotes the position of the border between the electron inflow and outflow channels, while the electron density cavity is signed by the blue dashed line.

electric field $E_{||}/V_AB_0$, and (c) the parallel electron bulk velocity $V_{e||}/V_A$ at $\Omega_i t = 31.4$, which is within the region associated with the left lower separatrix ($11 \le x/(c/\omega_{pi}) \le 22$ and $-3 \le z/(c/\omega_{pi}) \le -0.5$). Here the dotted curves mark the border between the electron inflow and outflow channels, while the dark purple region denotes the electron density cavity (the region with the electron density smaller than the nearby region). Obviously, the dotted curve (Figure 2b) passes through the region with the bipolar structures of the electric field. Figure 3 shows the profile of the parallel electric field $E_{||}/V_AB_0$ (the black curves), the parallel electron bulk velocity $V_{e||}/V_A$ (the red curves), and the electron number density n_e/n_0 (the blue curves) along the line $x = 17.1c/\omega_{pi}$ (which is denoted with the dashed line in Figure 2b) at $\Omega_i t = 31.4$. The red dashed line in Figure 3 denotes the position of the border of the electron inflow and outflow channels, while the electron density cavity is signed by the blue dashed line. The electrons flow to the X line inside the electron density cavity as reported previously [*Pritchett*, 2001; *Lu et al.*, 2010], while the bipolar structures of the electric field are found to be located in the border between the electron inflow and outflow channels in this paper. Obviously, the bipolar structures of the electric field are closer to the center of the plasma sheet than the electron density cavity. The distance in the z direction between the center of the bipolar structures (the peak of $E_{||}$) and the electron density cavity is about 0.3 c/ω_{pi}, while the width of the bipolar structure is about 0.5 c/ω_{pi}. Based on the local electron number density $n_L \sim 0.18n_0$, the local electron inertial length $c/\omega_{pe,L}$ is an estimated 0.3 c/ω_{pi}. Therefore, the width of the bipolar structures of the electric field is on the scale of the local electron inertial length, and it is related to electron dynamics.

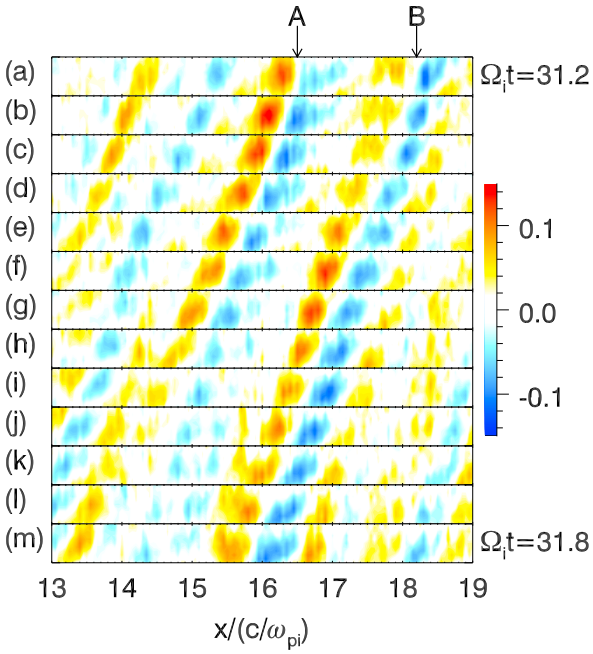

Figure 4. The propagation of the bipolar electric field structures along the magnetic field lines at the inner side of the left lower separatrix during the time interval $\Omega_i t = 31.2$ to 31.8 from top o bottom.

The propagation of the bipolar structures of the electric field can be analyzed based on Figure 4, which plots the time evolution of the parallel electric field $E_{||}/V_AB_0$ between the interval $31.2 \le \Omega_i t \le 31.8$ from top to down (the time interval between the contiguous snapshots is $0.05\Omega_i^{-1}$, about 5 times the local electron plasma period $\omega_{pe,L}^{-1}$). The parallel electric field is obtained from the red box denoted in Figure 2b, and it describes the propagation of the bipolar structures of the electric field around the left lower separatrix. In the figure, two obvious bipolar structures, which are denoted as A and B, can be easily identified. They propagate away from the X line along the magnetic field lines at the inner side of the separatrix with a nearly constant speed (~5 V_A). The magnitude of the bipolar structure A is decreasing, and the structure almost disappears at $\Omega_i t = 31.55$

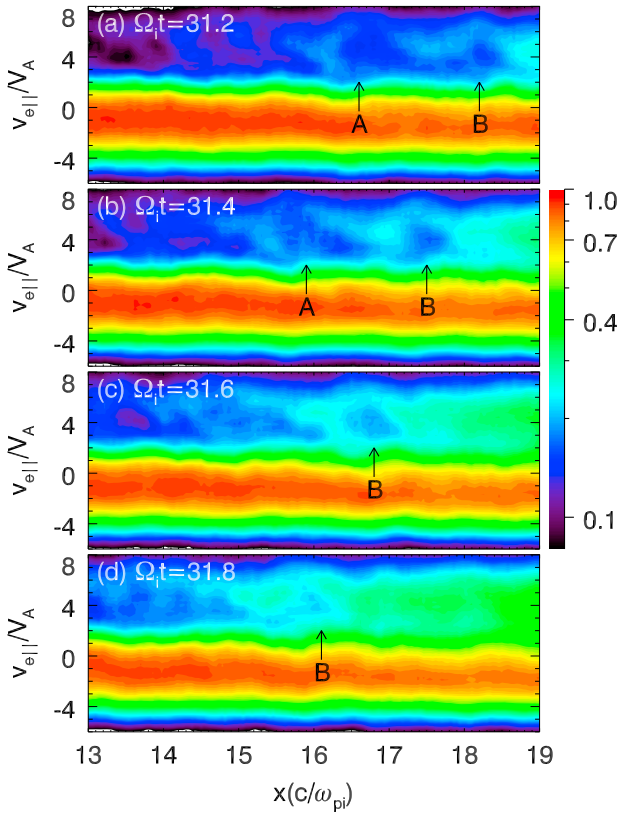

Figure 5. The time evolution of the electron distribution in the phase space $(x, v_{e||})$ along the profile (the red box in Figure 2b) near the left lower separatrix.

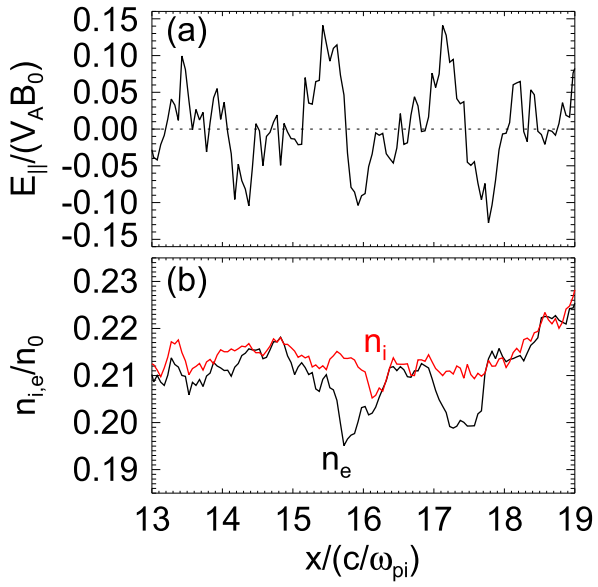

Figure 6. The (a) parallel electric field $E_{||}/V_A B_0$ and (b) ion and electron densities $n_{i,e}/n_0$ (red and black curves, respectively) along $z = -1.6c/\omega_{pi}$ at $\Omega_i t = 31.4$.

(denoted by "h"), while the magnitude of the structure B is increasing and reaches the peak at $\Omega_i t = 31.45$ (denoted by "f"). The typical magnitude of a characteristic bipolar structure of the electric field is around 0.1 $V_A B_0$, which is comparable to the reconnection electric field around the X line. In summary, the bipolar structures of the electric field have a large amplitude, and their scale is of the local electron inertial length; simultaneously, they are propagating away from the X line along the magnetic field lines at the inner side of the separatrices.

Figure 5 plots the time evolution of the electron phase-space $(x, v_{e||})$ distribution at (a) $\Omega_i t = 31.2$, (b) $\Omega_i t = 31.4$, (c) $\Omega_i t = 31.6$, and (d) $\Omega_i t = 31.8$. The distribution is calculated by taking from the red box denoted in Figure 2b. Compared with Figure 4, it is not difficult to find that the bipolar structures of the electric field correspond to the holes in the electron phase space, which are denoted by A and B in the figure. These electron phase-space holes propagate away from the X line along the magnetic field lines. Electron hole A is hardly recognizable from $\Omega_i t = 31.6$, while electron hole B is more stable and can be distinguished during the observation time. Figure 6a shows the bipolar structures of $E_{||}$ along $z = -1.6c/\omega_{pi}$ at $\Omega_i t = 31.4$, which result from the electrostatic potential caused by the lower electron number density relative to the ion number density shown in Figure 6b. The ion and electron densities are plotted by the red and black curves, respectively. The ion density changes little, and the bipolar structures of the parallel electric field are determined by the electron density. Therefore, the bipolar structures of the electric field belong to electron holes, which are related to electron dynamics.

The parallel velocity distribution of the electrons $f(v_{||})$ in the region $19.4c/\omega_{pi} \le x \le 19.8c/\omega_{pi}$, $-1.3c/\omega_{pi} \le z \le -0.9c/\omega_{pi}$ at $\Omega_i t = 29.3$ is given by the black curve in Figure 7. The red curve is the double-Gaussian fit of the black curve.
The distribution consists of two populations:

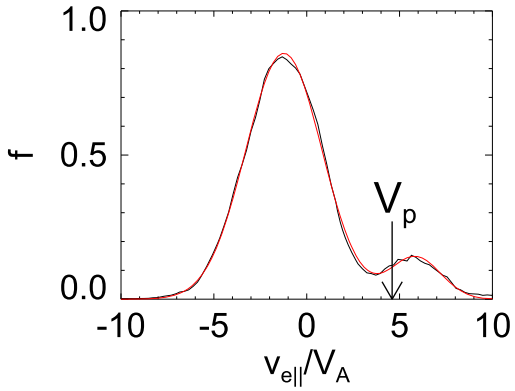

Figure 7. The black curve plots the electron parallel velocity distribution $f(v_{||})$ in the region $19.4c/\omega_{pi} \le x \le 19.8c/\omega_{pi}$, $1.3c/\omega_{pi} \le z \le -0.9c/\omega_{pi}$ (include the border between the electron inflow and outflow channels) at $\Omega_i t = 29.3$, while the red one is the corresponding double-Gaussian fit.

the majority is moving toward the X line, while the minority is away from the X line after they are accelerated in the vicinity of the X line. The bulk velocities of the outflow and inflow electrons are estimated to be about 6 V_A and -1.5 V_A, respectively, while the thermal velocity is about 2 V_A for both the inflow and outflow electrons. The drift velocity between the inflow and outflow is 7.5 V_A, which is much larger than the thermal velocity. The percentage of the faster outflow electrons is about 15%. Obviously, it is a bump-on-tail distribution. The generation of electron holes during the nonlinear evolution of the bump-on-tail instability has been reported in the previous researches [*Omura et al.*, 1996; *Lu et al.*, 2005b].

Figure 8 shows the time evolution of $E_{||}$ at the center of the structures along the x direction from $\Omega_i t = 29.3$ to $\Omega_i t = 31.8$. The waves begin to be excited by the bump-on-tail instability at about $\Omega_i t = 29.3$, and they are monochromatic until to about $\Omega_i t = 30.5$. They propagate along the $-x$ direction, which is away from the X line. From $\Omega_i t = 30.9$, the waves begin to coalesce with the neighboring ones. The process of the coalescent is denoted by the red and blue curves in Figure 8b. At $\Omega_i t = 31.4$, the coalescence is almost completed and the bipolar structures of $E_{||}$ are formed.

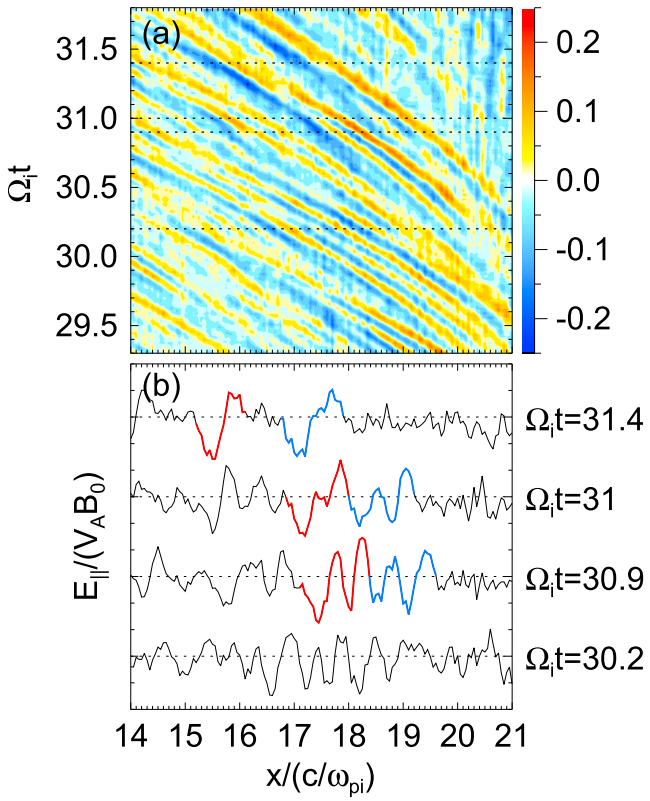

Figure 8. (a) The time evolution of parallel electric field $E_{||}/V_A B_0$ profile along the x direction from $\Omega_i t = 29.3$ to $\Omega_i t = 31.8$ and (b) the time profiles of $E_{||}/V_A B_0$, at $\Omega_i t = 30.2$, 30.9, 31, and 31.4. The two pairs of waves denoted with the red and blue curves coalesce to form the electron holes marked by A and B in Figures 4 and 5.

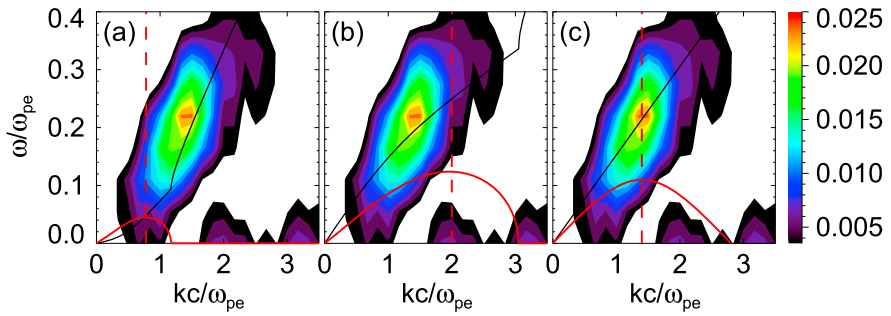

Figure 9. Wave spectrum of parallel electric field $E_{||}/V_A B_0$ (filled contours). The sampling region is $17.5c/\omega_{pi} \le x \le 20c/\omega_{pi}$, and the time interval is $29.3\Omega_i^{-1} \le t \le 30.2\Omega_i^{-1}$. The black and red curves are the theoretical profiles of the wave frequency ω_r/ω_{pe} and growth rate γ/ω_{pe}, respectively, deduced from the linear analyses of (a) the Buneman instability, (b) the cold electron two-stream instability, and (c) the bump-on-tail instability. The red dashed lines present the wave number corresponding to the maximum growth rate. By the fit curve in Figure 7, the drift velocities of the outflow and inflow populations are estimated to be about 6 V_A and -1.5 V_A, respectively, while the thermal velocity is about 2 V_A for both the inflow and outflow populations.

Theoretically, the waves excited by the Buneman instability and cold electron two-stream instability have the dispersion relations at the linear stage as

$$D = 1 - (n_L/n_0)\omega_{pe}^2 \left[\frac{m_e/m_i}{\omega^2} + \frac{\varepsilon}{(\omega - kv_{bo})^2} \right] = 0, \tag{1}$$

and

$$D = 1 - (n_L/n_0)\omega_{pe}^2 \left[\frac{1-\varepsilon}{(\omega - kv_{bi})^2} + \frac{\varepsilon}{(\omega - kv_{bo})^2} \right] = 0, \tag{2}$$

where $\varepsilon = 0.15$ and $v_{bo}/V_A = 6$ is the proportion and drift velocity of the minority outflow electrons; $v_{bi}/V_A = -1.5$ is the drift velocity of the main inflow electrons; $n_L/n_0 = 0.18$ is the local plasma number density; and $\omega = \omega_r + i\gamma$, where ω_r and γ present the real frequency and the growth rate. When the kinetic effects of electrons cannot be neglected, the dispersion relation of the bump-on-tail instability should be given by

$$D = 1 - \frac{n_L}{n_0} \frac{\omega_{pe}^2}{k^2 v_{to}^2} \left[(1-\varepsilon) \frac{v_{to}^2}{v_{ti}^2} Z'(\zeta_i) + \varepsilon Z'(\zeta_o) \right] = 0, \tag{3}$$

where v_{ti} and v_{to} are the thermal velocities of the inflow and outflow electrons, respectively. $\zeta_{i,o}$ is defined as $\zeta_{i,o} = (\omega/k - v_{bi,bo})/v_{ti,to}$. $Z(\zeta)$ is the plasma dispersion function expressed as

$$Z(\varsigma) = \frac{1}{\sqrt{\pi}} \int_{-\infty}^{+\infty} \frac{e^{-x^2} dx}{x - \varsigma}. \tag{4}$$

The dispersion function can be dealt with using the method proposed by *Roennmark* [1982], while equations (1)–(3) can be solved numerically by the full-matrix approach proposed by *Xie* [2013]. Figures 9a–9c show the theoretical profiles of the wave frequency (ω_r) and growth rates (γ) of the Buneman instability, cold electron two-stream instability, and bump-on-tail instability. The wave spectrums of $E_{||}$ in the (ω/ω_{pe}, kc/ω_{pe}) space are presented by the filled contours in Figure 9. The sampling region is $17.5c/\omega_{pi} \le x \le 20c/\omega_{pi}$, and the time interval is $29.3\Omega_i^{-1} \le t \le 30.2\Omega_i^{-1}$. During this interval, the waves are in the linear stage of the evolution. Note that the phase speed of cold electron two-stream instability varies during the later nonlinear evolution of the instability [*Che et al.*, 2009]. It is found that the spectrum has a clear peak around $\omega/\omega_{pe} \approx 0.21$ and $kc/\omega_{pe} \approx 1.4$. The phase speed is about 4.6 V_A. The theoretical frequency and wave number, where the growth rate of the Buneman instability reaches the maximum, are much smaller than those corresponding to the peak of the wave spectrum. In the cold electron two-stream instability, the theoretical wave number ($kc/\omega_{pe} \approx 2$) corresponding to the maximum growth rate is larger than that of the simulation result ($kc/\omega_{pe} \approx 1.4$), while the theoretical phase velocity ($v_p \approx 3.6V_A$) of the wave is smaller than that of the simulation result ($v_p \approx 4.6V_A$). The wave spectrum obtained in our simulations is consistent with the theoretical results of the bump-on-tail instability.

According to the theory, the maximum growth rate of bump-on-tail instability is $\gamma_{max} \approx 0.11\omega_{pe}$, and the corresponding frequency and wave number are $\omega/\omega_{pe} \approx 0.21$ and $kc/\omega_{pe} \approx 1.4$, respectively. Therefore, the corresponding wave length and phase speed are 0.56 c/ω_{pi} and 4.5 V_A, which are consistent with the simulation results.

In summary, after analyzing the formation of these electron holes observed in the border between the electron inflow and outflow channels, such as the earlier electron velocity distribution, and dispersion relation of the corresponding linear waves, we attribute the generation mechanism of these electron holes to be the nonlinear evolution of the electron bump-on-tail instability in the separatrix region during the antiparallel magnetic reconnection.

4. Conclusions and Discussion

Previous simulations [*Huang et al*., 2010; *Wang et al*., 2010] of antiparallel magnetic reconnection have shown that electrons in the diffusion region flow toward the X line along the separatrices due to the mirror effect, which lead to the generation of the electron density cavities along the separatrices. These electrons get accelerated by the reconnection electric field in the vicinity of the X line and then flow out along the magnetic field lines at the inner side of the separatrices. The formed in-plane electron currents result in the quadruple structure of the out-of-plane Hall magnetic field [*Sonnerup*, 1979; *Terasawa*, 1983; *Birn et al*., 2001; *Shay et al*., 2001; *Øieroset et al*., 2001; *Pritchett*, 2001; *Nagai et al*., 2003; *Fu et al*., 2006; *Retino et al*., 2006; *Lu et al*., 2010]. In this paper, by performing 2-D PIC simulations of antiparallel magnetic reconnection, we investigate the detailed characteristics of the electron holes in the separatrix region. The electron holes are identified in the border between the inflow and outflow electron channels, whose parallel electric field has bipolar structures along the magnetic field lines. The magnitude of the parallel electric field of the electric field is as strong as the reconnection field in the vicinity of the X line, and their width is on the scale of the local electron inertial length. The lifetime of these electron holes is estimated to be thousands of the local electron plasma periods, which is consistent with that of the electron holes in a homogeneous plasma [*Lu et al*., 2005a, 2008; *Wu et al*., 2010].

Moreover, in the region with the existence of the electron holes, the electrons are found to satisfy bump-on-tail distribution, where the inflow and outflow electrons consist of the background and the fast streaming electrons, respectively. At first, quasi-monochromatic electrostatic waves are first excited by the electron bump-on-tail instability. These waves then coalesce with each other, and at last several electron holes are generated. These electron holes propagate away from the X line along the magnetic field lines at the inner side of the separatrix region, and the propagation speed is nearly the bulk velocity of the fast outflow population. Such a generation process of electron holes is similar to that during the nonlinear evolution of the bump-on-tail instability in a homogeneous plasma [*Omura et al*., 1996]. Therefore, we conclude that the electron holes identified in this paper are the results of the nonlinear evolution of the bump-on-tail instability. With 2-D PIC simulations, *Fujimoto and Machida* [2006] also investigate the electron holes in the separatrix region during antiparallel reconnection, and they attributed the formation of the electron holes to the cold electron two-stream instability. The difference may be caused due to the different electron temperatures used between our simulations and that of *Fujimoto and Machida* [2006]. *Omura et al*. [1994, 1996] compared the generation of electron holes during the nonlinear evolution of both the cold electron two-stream instability and bump-on-tail instability. Electron holes can be formed in the cold electron two-stream instability only when the density of the electron beam is comparable to that of the background electrons, and their propagation speed is much smaller than the bulk velocity of the electron beam. However, electron holes can be formed in the bump-on-tail instability even if the density of the electron beam is much smaller than that of the background electrons, and their propagation speed is nearly the bulk velocity of the electron beam. Therefore, electron holes should be easy to be formed in the bump-on-tail instability and applied in space plasma [*Omura et al*., 1999]

In our simulation, a Harris current is used, while in reality the current sheet in the magnetotail is sandwiched by low dense tenuous lobes in the magnetotail. However, it will not change the pattern of the electron flow in antiparallel magnetic reconnection: the electrons move toward the X line along the separatrices, and they are directed away from the X line just inside the separatrices. Such a pattern of the electron flow has been observed in reconnection events in the magnetotail [*Wang et al*., 2010]. Therefore, the electron bump-on-tail distribution and electron holes should be able to be observed in the magnetotail. Actually, the

bump-on-tail distribution associated with electron holes has been observed in the magnetotail reconnection by Cluster [*Cattell et al*., 2005]. However, due to the limitation of the resolution, it is difficult to identify the exact mechanism of the electron holes observed by the satellite. NASA's Magnetospheric Multiscale Mission [*Sharma and Curtis*, 2005] will use four identical spacecraft to examine the process of magnetic reconnection. It will provide higher-resolution data for fields and particle distribution, which may give us a great chance to reveal the generation mechanism of electron holes during magnetic reconnection.

Acknowledgments

This research was supported by the National Science Foundation of China, grants 11220101002, 41204103, 11235009, 41274144, and 41121003; 973 Program (2013CBA01503 and 2012CB825602); Ph.D. Programs Foundation of Ministry of Education of China (20123402120010); the Specialized Research Fund for State Key Laboratories; CAS Key Research Program KZZD-EW-01-4; and the open research fund from SOA Key Laboratory for Polar Science (KP201205). The results in this paper are generated from our computer simulation code as described in section 2. The data can be obtained by contacting the authors through email (qmlu@ustc.edu.cn).

Larry Kepko would like to thank the reviewers for their assistance in evaluating this paper.

References

Bernstein, I. B., J. M. Greene, and M. D. Kruskal (1957), Exact nonlinear plasma oscillations, *Phys. Rev.*, *108*, 546–550.

Birn, J., et al. (2001), Geospace Environmental Modeling (GEM) magnetic reconnection challenge, *J. Geophys. Res.*, *106*(A3), 3715–3719, doi:10.1029/1999JA900449.

Cattell, C., J. Crumley, J. Dombeck, J. Wygant, and F. S. Mozer (2002), Polar observations of solitary waves at Earth's magnetopause, *Geophys. Res. Lett.*, *29*(5, 1065), doi:10.1029/2001GL014046.

Cattell, C., et al. (2005), Cluster observations of electron holes in association with magnetotail reconnection and comparison to simulations, *J. Geophys. Res.*, *110*, A01211, doi:10.1029/2004JA010519.

Che, H., J. F. Drake, M. Swisdak, and P. H. Yoon (2009), Nonlinear development of streaming instabilities in strongly magnetized plasma, *Phys. Rev. Lett.*, *102*(14), 145004, doi:10.1103/PhysRevLett.102.145004.

Chen, L. J., J. Pickett, P. Kintner, J. Franz, and D. Gurnett (2005), On the width-amplitude inequality of electron phase-space holes, *J. Geophys. Res.*, *110*, A09211, doi:10.1029/2005JA011087.

Drake, J. F., M. Swisdak, C. Cattell, M. A. Shay, B. N. Rogers, and A. Zeiler (2003), Formation of electron holes and particle energization during magnetic reconnection, *Science*, *299*, 873–877, doi:10.1126/science.1080333.

Ergun, R. E., C. W. Carlson, J. P. McFadden, and F. S. Mozer (1998), Fast satellite observations of large-amplitude solitary structures, *Geophys. Res. Lett.*, *25*(12), 2041–2044, doi:10.1029/98GL00636.

Fox, W., M. Porkolab, J. Egedal, N. Katz, and A. Le (2008), Laboratory observation of electron phase-space holes during magnetic reconnection, *Phys. Rev. Lett.*, *101*, 255003, doi:10.1103/PhysRevLett.101.255003.

Fu, X. R., Q. M. Lu, and S. Wang (2006), The process of electron acceleration during collisionless magnetic reconnection, *Phys. Plasmas*, *13*, 012309.

Fujimoto, K., and S. Machida (2006), A generation mechanism of electrostatic waves and subsequent electron heating in the plasma sheet-lobe boundary region during magnetic reconnection, *J. Geophys. Res.*, *111*, A09216, doi:10.1029/2005JA011542.

Goldman, M. V., D. L. Newman, and P. Pritchett (2008), Vlasov simulations of electron holes driven by particle distributions from PIC reconnection simulations with a guide field, *Geophys. Res. Lett.*, *35*, L22109, doi:10.1029/2008GL035608.

Goldman, M. V., D. L. Newman, G. Lapenta, L. Andersson, J. T. Gosling, S. Eriksson, S. Markidis, J. P. Eastwood, and R. Ergun (2014), Čerenkov emission of quasiparallel whistlers by fast electron phase-space holes during magnetic reconnection, *Phys. Rev. Lett.*, *112*, 145002, doi:10.1103/PhysRevLett.112.145002.

Hoshino, M., T. Mukai, T. Terasawa, and I. Shinohara (2001), Suprathermal electron acceleration in magnetic reconnection, *J. Geophys. Res.*, *106*, 25,979–25,997, doi:10.1029/2001JA900052.

Huang, C., Q. M. Lu, and S. Wang (2010), The mechanisms of electron acceleration in antiparallel and guide field magnetic reconnection, *Phys. Plasmas*, *17*, 072306, doi:10.1063/1.3457930.

Khotyaintsev, Y. V., A. Vaivads, M. Andre, and M. Fujimoto (2010), Observations of slow electron holes at a magnetic reconnection site, *Phys. Rev. Lett.*, *105*, 165002.

Lapenta, G., S. Markidis, A. Divin, M. Goldman, and D. Newman (2010), Scales of guide field reconnection at the hydrogen mass ratio, *Phys. Plasmas*, *17*(8, 082106), doi:10.1063/1.3467503.

Lapenta, G., S. Markidis, A. Divin, M. V. Goldman, and D. L. Newman (2011), Bipolar electric field signatures of reconnection separatrices for a hydrogen plasma at realistic guide fields, *Geophys. Res. Lett.*, *38*, L17104, doi:10.1029/2011GL048572.

Lu, Q. M., D. Y. Wang, and S. Wang (2005a), Generation mechanism of electrostatic solitary waves in the Earth's auroral region, *J. Geophys. Res.*, *110*, A03223, doi:10.1029/2004JA010739.

Lu, Q. M., S. Wang, and X. K. Dou (2005b), Electrostatic waves in an electron-beam plasma system, *Phys. Plasmas*, *12*, 072903.

Lu, Q. M., B. Lembege, J. B. Tao, and S. Wang (2008), Perpendicular electric field in two-dimensional electron phase-holes: A parameter study, *J. Geophys. Res.*, *113*, A11219, doi:10.1029/2008JA013693.

Lu, Q. M., C. Huang, J. L. Xie, R. S. Wang, M. Y. Wu, A. Vaivads, and S. Wang (2010), Features of separatrix regions in magnetic reconnection: Comparison of 2-D particle-in-cell simulations and Cluster observations, *J. Geophys. Res.*, *115*, A11208, doi:10.1029/2010JA015713.

Mangeney, A., C. Salem, C. Lacombe, J. L. Bougeret, C. Perche, R. Manning, P. J. Kellogg, K. Goetz, S. J. Monson, and J. M. Bosqued (1999), WIND observations of coherent electrostatic waves in the solar wind, *Ann. Geophys.*, *17*, 307–320.

Matsumoto, H., H. Kojima, T. Miyatake, Y. Omura, M. Okada, I. Nagano, and M. Tsutsui (1994), Electrostatic solitary waves (ESW) in the magnetotail: BEN wave forms observed by Geotail, *Geophys. Res. Lett.*, *21*(25), 2915–2918, doi:10.1029/94GL01284.

Morse, R. L., and C. W. Nielson (1969), One-, two-, and three-dimensional numerical simulation of two-beam plasmas, *Phys. Rev. Lett.*, *23*, 1087–1089.

Mottez, F., S. Perraut, A. Roux, and P. Louarn (1997), Coherent structures in the magnetotail triggered by counterstreaming electron beams, *J. Geophys. Res.*, *102*(A6), 11,399–11,408, doi:10.1029/97JA00385.

Muschietti, L., R. E. Ergun, I. Roth, and C. W. Carlson (1999), Phase-space electron holes along magnetic field lines, *Geophys. Res. Lett.*, *26*(8), 1093–1096, doi:10.1029/1999GL900207.

Nagai, T., I. Shinohara, M. Fujimoto, S. Machida, R. Nakamura, Y. Saito, and T. Mukai (2003), Structure of the Hall current system in the vicinity of the magnetic reconnection site, *J. Geophys. Res.*, *108*, 1357, doi:10.1029/2003JA009900.

Ng, C. S., and A. Bhattacharjee (2005), Bernstein-Greene-Kruskal modes in a three-dimensional plasma, *Phys. Rev. Lett.*, *95*, 245004.

Øieroset, M., T. D. Phan, M. Fujimoto, R. P. Lin, and R. P. Lepping (2001), In situ detection of collisionless reconnection in the Earth's magnetotail, *Nature*, *412*, 414–417, doi:10.1038/35086520.

Omura, Y., H. Kojama, and H. Matsumoto (1994), Computer simulation of electrostatic solitary waves: A nonlinear model of broadband electrostatic noise, *Geophys. Res. Lett.*, *21*(25), 2923–2926, doi:10.1029/94GL01605.

Omura, Y., H. Matsumoto, T. Miyake, and H. Kojima (1996), Electron beam instabilities as generation mechanism of electrostatic solitary waves in the magnetotail, *J. Geophys. Res.*, *101*, 2685–2697, doi:10.1029/95JA03145.

Omura, Y., H. Kojima, N. Miki, T. Mukai, H. Matsumoto, and R. Anderson (1999), Electrostatic solitary waves carried by diffused electron beams observed by the Geotail spacecraft, *J. Geophys. Res.*, *104*, 14,627–14,637, doi:10.1029/1999JA900103.

Pickett, J. S., L. J. Chen, S. W. Kahler, O. Santolik, D. A. Gurnett, B. T. Tsurutani, and A. Balogh (2004), Isolated electrostatic structures observed throughout the cluster orbit: Relationship to magnetic field strength, *Ann. Geophys.*, *22*, 2525–2523.

Pritchett, P. L. (2001), Geospace Environment Modeling magnetic reconnection challenge: Simulations with a full particle electromagnetic code, *J. Geophys. Res.*, *106*(A3), 3783–3798, doi:10.1029/1999JA001006.

Pritchett, P. L., and F. V. Coroniti (2004), Three-dimensional collisionless magnetic reconnection in the presence of a guide field, *J. Geophys. Res.*, *109*, A01220, doi:10.1029/2003JA009999.

Retino, A., et al. (2006), Structure of the separatrix region close to a magnetic reconnection X-line: Cluster observations, *Geophys. Res. Lett.*, *33*, L06101, doi:10.1029/2005GL024650.

Roennmark, K. (1982), Computation of the dielectric tensor of a Maxwellian plasma, *Plasma Phys.*, *25*, 699–701, doi:10.1088/0032-1028/25/6/007.

Sharma, A. S., and S. A. Curtis (2005), *Magnetospheric Multiscale Mission*, Astrophys. Space Sci. Libr., vol. 321, pp. 179–195, Springer, Dordrecht, Netherlands.

Shay, M. A., J. F. Drake, B. N. Rogers, and R. E. Denton (2001), Alfvénic collisionless magnetic reconnection and the Hall term, *J. Geophys. Res.*, *106*, 3759–3772, doi:10.1029/1999JA001007.

Sonnerup, B. U. Ö. (1979), Magnetic field reconnection, in *Solar System Plasma Physics*, vol. 3, edited by L. J. Lanzèerotti, C. F. Kennel, and E. N. Parker, pp. 45–108, North-Holland, New York.

Terasawa, T. (1983), Hall current effect on tearing mode instability, *Geophys. Res. Lett.*, *10*, 475–478, doi:10.1029/GL010i006p00475.

Wang, R. S., Q. M. Lu, C. Huang, and S. Wang (2010), Multispacecraft observation of electron pitch angle distributions in magnetotail reconnection, *J. Geophys. Res.*, *115*, A01209, doi:10.1029/2009JA014553.

Wu, M., Q. Lu, C. Huang, and S. Wang (2010), Transverse instability and perpendicular electric field in two-dimensional electron phase-space holes, *J. Geophys. Res.*, *115*, A10245, doi:10.1029/2009JA015235.

Xie, H. S. (2013), A full-matrix approach for solving general plasma dispersion relation, arXiv:1304.5885 [physics.plasm-ph].